Shearography pair method for reliable non-destructive inspection of millimeter and submillimeter defects in fiber-reinforced composites

Tao, Nan; Groves, Roger M.; Anisimov, Andrei G.

DOI
10.1016/j.measurement.2025.117980

Publication date
2025

Document Version
Final published version

Published in
Measurement: Journal of the International Measurement Confederation

Measurement 255 (2025) 117980

Contents lists available at ScienceDirect

Measurement

journal homepage: www.elsevier.com/locate/measurement

Shearography pair method for reliable non-destructive inspection of millimeter and submillimeter defects in fiber-reinforced composites

Nan Tao *, Roger M. Groves, Andrei G. Anisimov

Department of Aerospace Structures and Materials, Delft University of Technology Kluyverweg 1, 2629 HS Delft, the Netherlands

ARTICLE INFO

Keywords:
Non-destructive inspection (NDI)
Shearography pair method
Thermal loading
Fiber-related deformation
Sub-mm defect detection

ABSTRACT

Non-destructive inspection (NDI) of small-scale defects in fiber-reinforced composites is an urgent challenge to ensure the structural integrity of safety–critical components. Shearography is a non-contact and full-field optical NDI method that can be used to characterize surface strain components under loading. Thermal loading is widely used in shearography because of the advantages of being non-contact and convenient for in-service inspection. Shearography has received considerable industrial acceptance for the inspection of aerospace and marine composite structures, however its efficacies in detecting small mm and sub-mm defects have not been fully characterised. Besides, one major issue regarding shearography with thermal loading is fiber-related deformation or fiber noise, which can affect the efficacy of defect detection significantly, especially when detecting small and deep defects. In this study, the novel shearography pair method is proposed and developed to reduce fiber noise for reliable inspection of small mm and sub-mm defects in composites. The defect detection capabilities of the proposed method have been studied and compared with conventional shearography practice and with fast Fourier transform (FFT) and principal component analysis (PCA) based signal processing algorithms. The results demonstrate that the proposed shearography pair method has the advantages of less fiber noise, improved inspection results, and being faster with reduced number of datasets. It enables the detection of mm and sub-mm defects (down to 0.6–0.8 mm in diameter) in composites; these inspection results are one of the smallest defect sizes detected with shearography and reported in literature.

1. Introduction

Fiber-reinforced composites, such as carbon fiber-reinforced polymers (CFRP) and glass fiber-reinforced polymers (GFRP), have been increasingly adopted in safety–critical structures in the aerospace, marine and wind energy sectors over the last few decades [1–3]. Numerous types of defects and damage can occur in composite materials including delaminations, matrix cracking, fiber breakage and impact damage [3,4]. Non-destructive inspection (NDI) and defect detection in these composites are therefore critical to ensure structural integrity and safety. Particularly, inspection capabilities of small defects, for example in the mm and sub-mm range, have become increasingly important for the structural safety of critical components in high-value applications [5] such as composite liquid hydrogen tanks.

Among the different NDI techniques, digital shearography is a non-contact and full-field optical technique that has received considerable interest in various industries, in particular, for the inspection of aerospace and marine composite structures [6–8]. Shearography NDI methods can offer effective solutions for the detection of both manufacturing and in-service defects in composites such as delaminations, fiber breakage and impact damage [9]. Temporal phase-shifting shearography is commonly used due to high accuracy and is suitable for static and quasi-static measurements. The development of shearography techniques in recent years includes FEM-assisted shearography for thick marine composite inspection [8,10], shearography measurement and CT scans of delamination defects in composite hydrogen storage cylinders [11], 3D shearography for in-situ inspection of large canvas paintings [12], acoustic shearography for non-contact defect imaging composite materials and metallic coatings [13–16]. Nevertheless, the detection capabilities of shearography for small defects (e.g., in the mm and sub-mm scale) still need to be investigated.

Shearography can detect defects in an object as surface strain anomalies after a certain loading. The defect-induced surface strain anomalies are usually identified by comparing two deformation states of the test object. The two states are also known as the '**reference**' and '**signal**' states or speckle interferograms [7,17]. The outputs from

* Corresponding author.
E-mail address: n.tao@tudelft.nl (N. Tao).

https://doi.org/10.1016/j.measurement.2025.117980
Received 7 March 2025; Received in revised form 10 May 2025; Accepted 26 May 2025
Available online 28 May 2025

shearography include phase maps (ϕ), which can be related to the in-plane and out-of-plane surface strain components of the test object. A key objective in shearography NDI is selecting a load to deform the test structure to achieve a reasonable defect deformation (e.g., by a few micro-strains). Common loading methods for shearography include pressure [11,18–20], vacuum [21–23], mechanical [16,24], vibration [13,14,25,26], and thermal [8,27–29] loadings. A summary of different loading-based shearography techniques is shown in Table 1. Based on the literature survey, previous studies have generally been limited to defect sizes of 3–20 mm in metals and 5–120 mm in composite materials. To the best of our knowledge, the study on shearography detection of small mm (e.g., size of 1–3 mm) and sub-mm size internal defects in composite laminates is still very limited [19,20].

Among the different loadingings, thermal loading is widely used [7,9,17,30–32] because of the advantages of being non-contact and convenient for in-service inspection. However one major issue is fiber-related deformations, which arise from the difference in thermal conductivity and thermal expansion coefficient between the reinforcing fiber and matrix. These fiber-related deformations can affect the efficacy of defect detection significantly, especially when measuring small and deep defects [10,29]. Moreover, the presence of various layup sequences can cause significant changes in heat propagation through the composites, causing non-uniform deformation background that poses difficulties and challenges in defect detection and characterization. Examples of fiber deformation-related noise or fiber noise limiting the detection of small and deep defects in fiber-reinforced composites are given in Fig. 1. Successful detection of defects in the same specimen during the same test may be possible, if the fiber noise can be suppressed. This structured fiber-related deformation background, e.g., vertical and diagonal lines in Fig. 1(b,d), is a general issue among various fiber-reinforced composites including CFRP and GFRP. Similar phenomenon related to the fiber layup features/structures also occurs in thermography and eddy-current testing methods [33–35]. Hughes et al. determined the dominant fiber orientations present in the CFRP structure by applying radon-transform techniques for eddy-current data [33]. Poelman et al. separated the structured fiber background from the defect information by using k-space analysis of thermographic images obtained from the woven fabric composites [35]. Nevertheless, little attention has been paid to the analysis of fiber-related deformation to improve shearography NDI of fiber-reinforced composites with thermal loading.

Table 1
Summary of different loading-based shearography techniques for NDI.

Loading method	Description	Detectable defects
Pressure	Suitable for pressure vessels, pipes, honeycomb structures; Not suitable for solid laminates.	• In metals: flat bottom holes (FBHs) of 5–8 mm in size were detected in aluminum plates (at 0.5 mm defect depth) [18]. • In composites: delaminations down to 60 mm in size were detected in CFRP hydrogen storage cylinder [11]; voids of more than 1 mm in size were detected in high-pressure CFRP tube [19,20].
Vacuum	A vacuum test chamber is required. Suitable for testing of tires, composite laminates, and honeycombs. For larger objects, the total enclosure is not practical.	• In metals: defects of size less than 10 mm and depth larger than 0.5 mm were hardly detected [23]. • In composites: Teflon inclusions of 5–30 mm in size were detected in GFRP plates [21,22]; defects with less than 10 mm and depth larger than 0.5 mm were hardly detected in CFRP plates [23].
Mechanical	A loading machine (e.g., tensile machine) is usually needed; rigid body motion can be a problem.	• In composites: microcracks from a few mm to several tens of mm in length were detected in CFRP plates [16]; impact damage of size around 120 mm was detected in composite ship hull section [24].
Vibration	Contact may be required (e.g., using PZT excitation)	• In composites: FBHs of 20–40 mm in size were detected in CFRP plates [25]; microcracks of around 0.8–6 mm in length were detected in CFRP laminates [13,14].
Thermal	Heating sources such as halogen lamps are needed. Being non-contact, convenient, versatile and cost-effective for on-site inspection.	• In metals: FBHs of 3–8 mm diameter at 1–2.5 mm depth were detected [27]. • In composites: FBHs of 30–60 mm in size at up to 20–25 mm depth were detected. [8,29]; delaminations with a size of 10–30 mm were detected in a honeycomb panel [28]

It should be emphasized that the novelty of the work is not on improving the optical scheme, but on improving the performance of thermal-based shearography data processing for defect detection in composites. In the regular inspection practice, the signal and reference interferograms are captured at time moments, e.g. before excitation and after, without proper analysis of the object behaviour and deformations during the excitation. Potentially, defect detection with shearography could be enhanced by specially choosing pairs of speckle interferograms with similar level of fiber-induced noise. In this work, we are aiming to develop new shearography pair method by using specially chosen pairs of the signal and reference interferograms (with respect to the heating scenario) to minimize the fiber noise. Additionally, existing signal processing algorithms such as those based on fast Fourier transform (FFT) and principal component analysis (PCA) [36–40] are compared with the developed shearography pair method. The preliminary results of this research were reported earlier in conference proceedings [41].

The goal of this study is to push the boundaries of shearography inspection of composite materials towards sub-mm scale defects. For that, the shearography pair method has been proposed and developed through the analysis of fiber-induced deformation during heating and cooling. Shearography pairs are the pairs of reference and signal sets of phase-shifted speckle interferograms that yield minimum fiber noise for defect detection. The remainder of the article is organized as follows. Section 2 introduces the test CFRP specimen and shearography theory. Section 3 details the proposed shearography pair method. Section 4 presents shearography pair results and a comparison with conventional shearography practice including well-known signal processing algorithms, such as FFT and PCA. Conclusions are given in Section 5.

2. Test specimen and digital shearography

To highlight the performance of the developed shearography pair method, we focus on an experimental study of detecting small mm and sub-mm defects — flat bottom holes (FBHs). As manufacturing delaminations of sub-mm size is challenging, FBHs are used as reference defects to reliably simulate major defects of various sizes and depths in the composite laminate, following common practice in research papers [25,27,42] and industrial NDI applications [43,44].

2.1. Test CFRP specimen

The test specimen (Fig. 2) is a typical aerospace CFRP laminate made from CYCOM 977–2 by Cytec. The size of the specimen is 200 × 200 × 4 mm and its layup is $[0/90]_{5s}$. A series of flat bottom holes were milled in duplicate (twin defects) at the back surface of the plate at the center area. The diameters (dia) of the holes ranged from 0.4 to 3 mm and the remaining thickness (rem) varied from 1 to 3 mm, representing reference defects of various sizes and at different depths. To check for manufacturing errors, the holes of diameter of 0.8–3.0 mm with

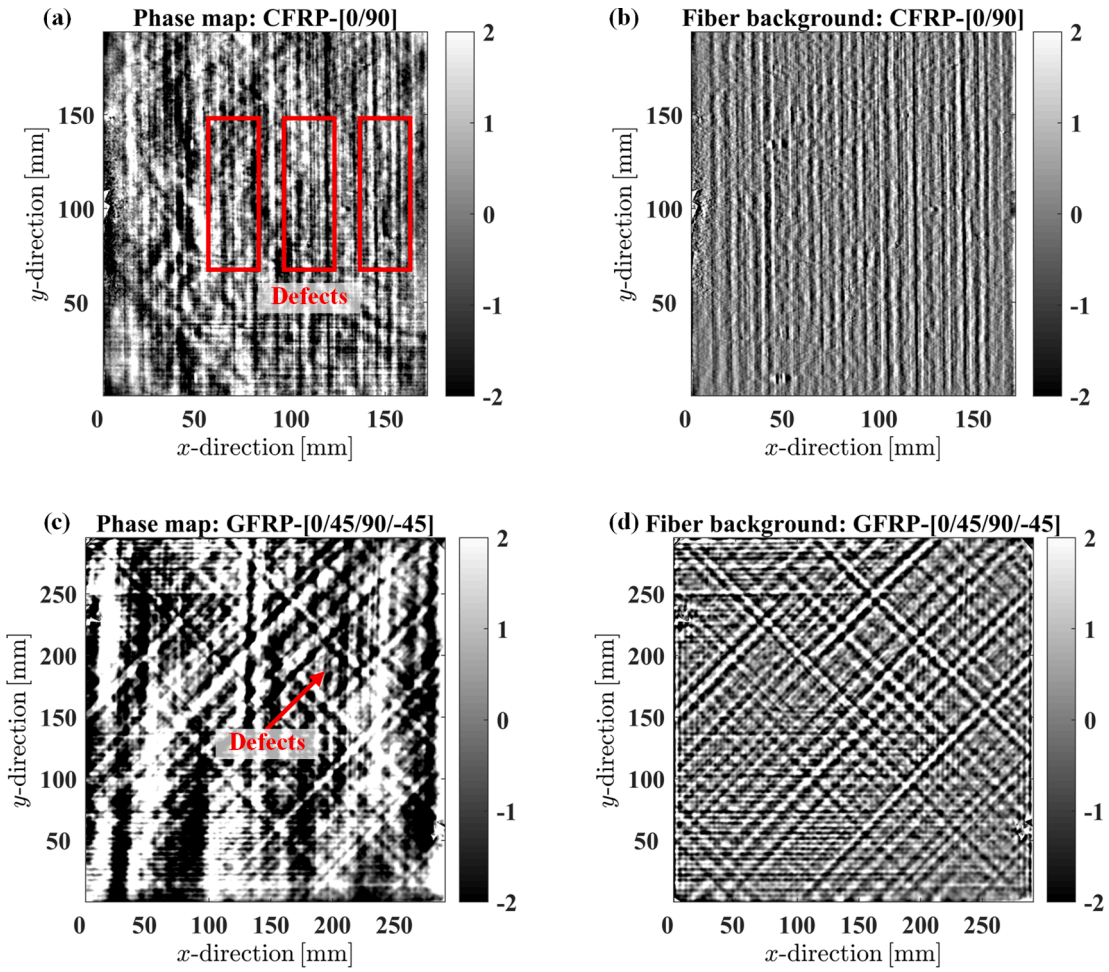

Fig. 1. (This figure is given to illustrate the problem without detailed description to keep the focus of this paper.) Examples of fiber noise limiting the detection of small and deep defects in fiber-reinforced composites. (a)-(b) Shearography results (phase maps ϕ, proportional to the out-of-plane displacement derivative $\partial w/\partial x$) of a 4-mm-thick aerospace CFRP laminate with 0.4–3 mm defects, the defects are not detected due to the fiber noise (a) with high fiber noise, and (b) its fiber background. Phase units in rad, 1 rad corresponds to 5.4 με. (c)-(d) Shearography results of a 51-mm-thick marine GFRP laminate with a defect at 25 mm depth, (c) with high fiber noise, and (d) its fiber background. 1 rad corresponds to 13.2 με.

remaining thickness of 1 mm were measured with a Keyence VK-X1000 confocal scanning microscope and the deviation (mean value) between measured dimensions vs. the nominal ones is within 0.06 mm.

2.2. Shearography instrument

A schematic of shearography is shown in Fig. 3(a). With the shearing device, the scattered laser light from two neighbouring positions on the specimen surface (separated by shearing distance δx) can interfere at the camera to produce the interferogram. The experimental system is shown in Fig. 3(b). The test CFRP laminate was inspected from the front surface (defect-free side) using one channel of a modified 3D shape shearography system [29,45] with a main focus on the out-of-plane deformation (Fig. 3(b)). This was achieved by placing the shearing camera close to parallel to the laser beam and perpendicular to the specimen (Fig. 3(a-b)). The selection of focusing on out-of-plane shearography was made as the out-of-plane deformation of delaminations and flat bottom holes is expected to be dominant.

The specimen was illuminated with a Torus 532 CW laser (Laser Quantum, wavelength λ of 532 nm, operating at around 100 mW optical power) through a beam expander, creating a speckle interferograms. The front surface of the specimen (defect-free side) was sprayed with removable white paint in matt finish to increase the amount of scattered laser light. The shearing camera included a Pilot piA2400 camera (2456 $\times$ 2058 pixels) by Basler with a Linos MeVis-C 1.6/25 lens and a spectral bandpass filter (center wavelength of 532 nm with bandpass of 4 nm). This shearing camera had a Michelson shearing interferometer with temporal phase-shifting realised by a piezo-electric actuator PSH 4z (Piezosystem Jena), enabling continuous recording of the phase-shifted sets of speckle interferograms. The four-step phase-shifting method was adopted due to its convenience [7], it was done by recording four speckle interferograms (each having $\pi/2$ phase-shift, i.e., 0, $\pi/2$, π, $3\pi/2$) in both reference and signal states. One full phase-shifting cycle takes about 3.5 s, which is relatively slow due to the low laser power (100 mW) and the limitation of the used piezoelectric transducer. It is acceptable for the laboratory conditions (including the clamping boundary condition). For industrial applications, fast phase-shifting (e.g., $<$ 1 s) is preferred.

The field of view (FOV) of the shearing camera was approximately 220 $\times$ 260 mm at 1 m distance. The shearing distance δx was calibrated over the FOV according to [45,46]. Different shearing distances (2.0–5.7 mm) were tested during the experiments. A suitable shearing distance of 3.2 mm on average (approximately 26–27 pixels, with 1 pixel corresponding to around 0.12 mm) in the horizontal direction (x-axis) was experimentally determined to obtain good number of fringes for phase unwrapping and sufficient sensitivity for defect detection.

During the inspection, two opposite edges of the specimen were clamped. Three halogen lamps (SUPER PAR CP62) operating at an

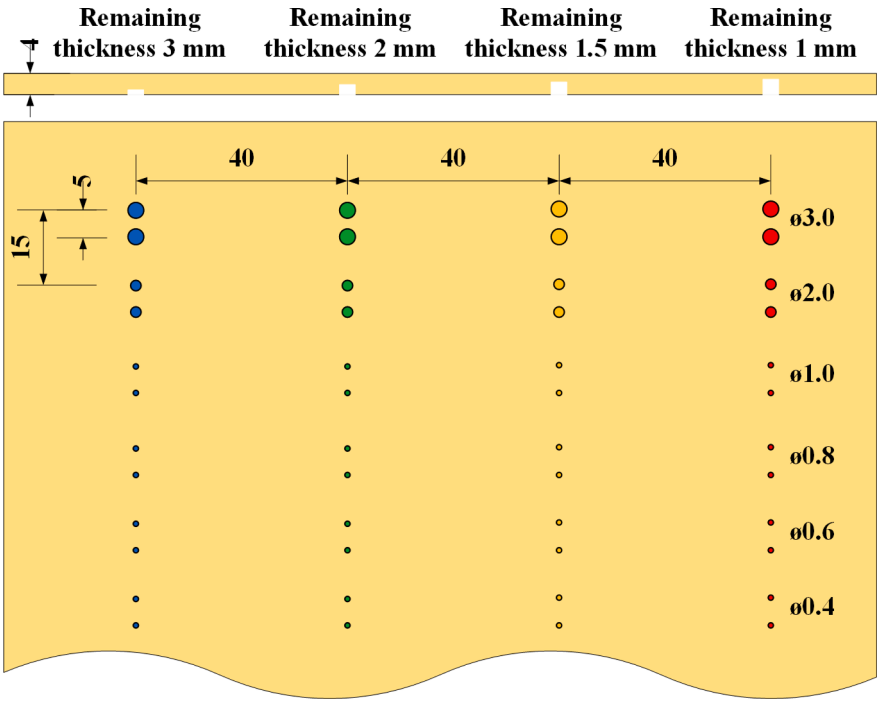

Fig. 2. Schematic of the test CFRP specimen with flat bottom holes (FBHs) at the center area. The FBHs were milled at the back surface of the specimen in duplicate (twin defects: two FBHs of the same size and at the same depth). [units in mm].

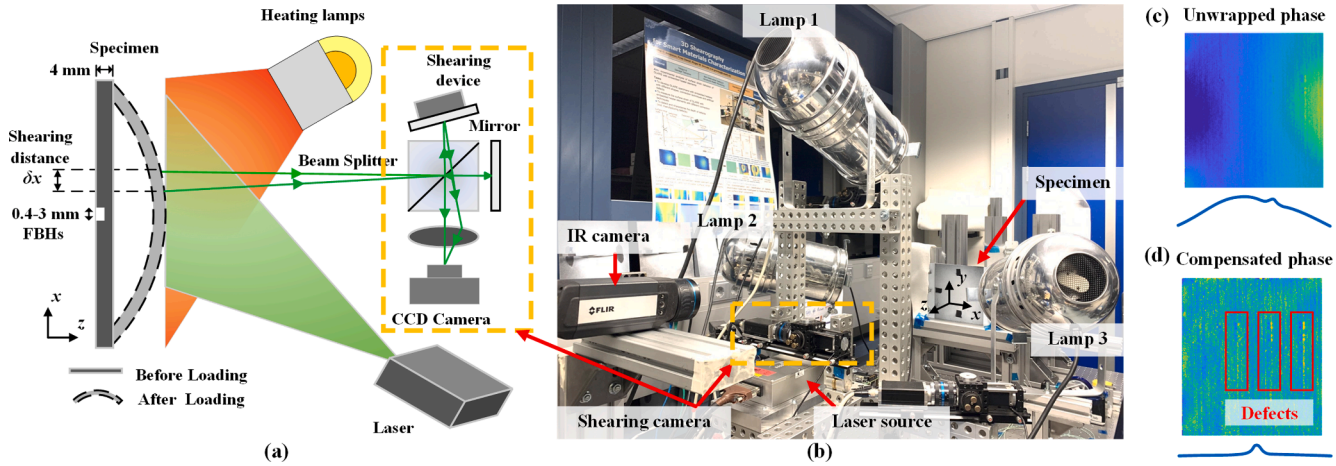

Fig. 3. (a) Schematic of shearography based on a Michelson interferometer. (b) The experimental system with the main focus on the out-of-plane deformation, the specimen is placed at a distance of approx. 1 m from the shearing camera. (c-d) Unwrapped and compensated phase maps.

electrical power of 500 W each were used to apply thermal loading to the specimen. The temperature on the front surface of the specimen (emissivity assumend to be 0.95 [47]) was monitored with a FLIR A655 IR camera (640 × 480 pixels, thermal sensitivity < 30 mK). The specimen was heated by 10 cycles of 30 s heating, resulting in a temperature rise of 40 °C. To enable the developing shearography pair method, measurements during heating have to be made in addition to the ones made before heating and during cooling. The optical filter used to pass the laser light (spectral bandpass filter) was found to be not efficient in blocking the light from the lamps, so the heating was off after each 30 s for the shearing camera to capture the phase-shifted interferograms. The overall amount of heat assures sufficient defect deformation for shearography NDI. The shearing camera (Fig. 3(a-b)) continuously captured sets of speckle interferograms before heating, at the short pauses between cycles of heating, and during cooling. All the sets of speckle interferograms (600 + datasets) were processed through temporal phase shifting (four-step), phase filtering and unwrapping to give phase map stack with respect to time. The filtering was sine/cosine filtered with iterative circular averaging and median filters with a radius of 2 pixels and an aperture of 3 × 3 pixels respectively. Phase unwrapping was done with the branch-cut method [48]. A phase compensation process (Fig. 3 (c-d)) by using polynomial fitting was further performed [8,10] to remove the phase change due to global deformation for the inspection.

3. Shearography pair method for non-destructive inspection

In this section, the new shearography pair method is developed through the analysis of fiber-related and defect deformation during heating and cooling. First, the variation of fiber-related phase and defect phase in time were investigated, then optimal shearography pairs, i.e., the pairs of reference and signal speckle interferograms that yield minimum fiber noise, were determined. In shearography, phase maps

(ϕ) are the primary outputs that can be obtained by computing phase differences of the speckle interferograms at two deformation states. The obtained phase is proportional to the out-of-plane displacement derivative in the shearing direction ($\phi = \frac{4\pi}{\lambda}\frac{\partial w}{\partial x}\delta x$), where λ is the laser wavelength and δx is the shearing distance [8]. In this paper radian is chosen as a unit for the phase analysis, and in this instrument-specimen geometry (Fig. 3(b)), 1 rad corresponds to 13.2 με. It should be noted that the phase maps were cropped to exclude the specimen clamping region.

3.1. The approach to identifying the fiber and defect-induced phases

In order to analyse the fiber-related and defect-induced deformations during the inspection, first the fiber phase and defect phase at each time instant need to be identified. This section introduces the approach to characterize the fiber and defect deformations.

It was found, that fiber deformation is the highest, if measured from before the heating to the end of the heating. To determine the fiber phase, a phase compensation process is needed to remove overall or global deformation, which can be done by subtracting the original phase map with the fitted surface created by a polynomial fitting to the original phase. The compensated phase map of total heating was obtained as shown in Fig. 4(a). Fiber deformation appears at the locations with local max or local min phase values. To find these locations, we plotted the phase changes of different cross-sections along three red lines in Fig. 4 (a). The three lines were selected randomly in defect-free areas to provide reliable statistical dataset. The positions of local max and min phases were extracted with a prominence window of 10 pixels along the three red horizontal lines (Fig. 4(d-f)). The points marked in red and blue are expected to be the positions of fiber bundles. A histogram of the local max and min phases from the fiber locations was plotted with a fitted normal distribution curve overlaid (Fig. 4(g)), showing the fiber-related phase distribution close to a normal distribution. The assumption of normal distribution was justified by testing for skewness and kurtosis (Table 2). As $|\text{Skewness}| < 0.5$ and $|\text{Kurtosis} - 3| < 1$, the data appears to approximately follow the normal distribution.

After identifying fiber positions (coordinate in pixels), the absolute values of the phases at those positions were averaged to represent fiber-related deformation (ϕ_{fiber} in Eq. (1)) at a time instant:

$$\phi_{\text{fiber}} = \frac{|\overline{\phi}_{\text{localmax}}| + |\overline{\phi}_{\text{localmin}}|}{2} \tag{1}$$

Where $\overline{\phi}_{\text{localmax}}$ is the average of all the local maximum values of the fiber-induced phase and $\overline{\phi}_{\text{localmin}}$ is the average of all the local minimum values of the fiber-induced phase (Fig. 6 (steps 2.2–2.3)) along the three red lines in Fig. 4, respectively. Then the average of $|\overline{\phi}_{\text{localmax}}|$ and $|\overline{\phi}_{\text{localmin}}|$ is computed and we assume the average of the absolute values ($|\overline{\phi}_{\text{localmax}}|$ and $|\overline{\phi}_{\text{localmin}}|$) to represent the fiber phase ϕ_{fiber} (Fig. 6 (steps 2.3–2.4)).

The same operation was done for each compensated phase map from 600 + datasets in the time sequence so that the evolution of the fiber-related deformation with time can be obtained (Fig. 5(b)). A

Table 2
skewness and kurtosis of the data.

	Skewness	Kurtosis
The maximum values of the fiber-induced phase	0.0561	3.1159
The minimum values of the fiber-induced phase	−0.4864	3.3766

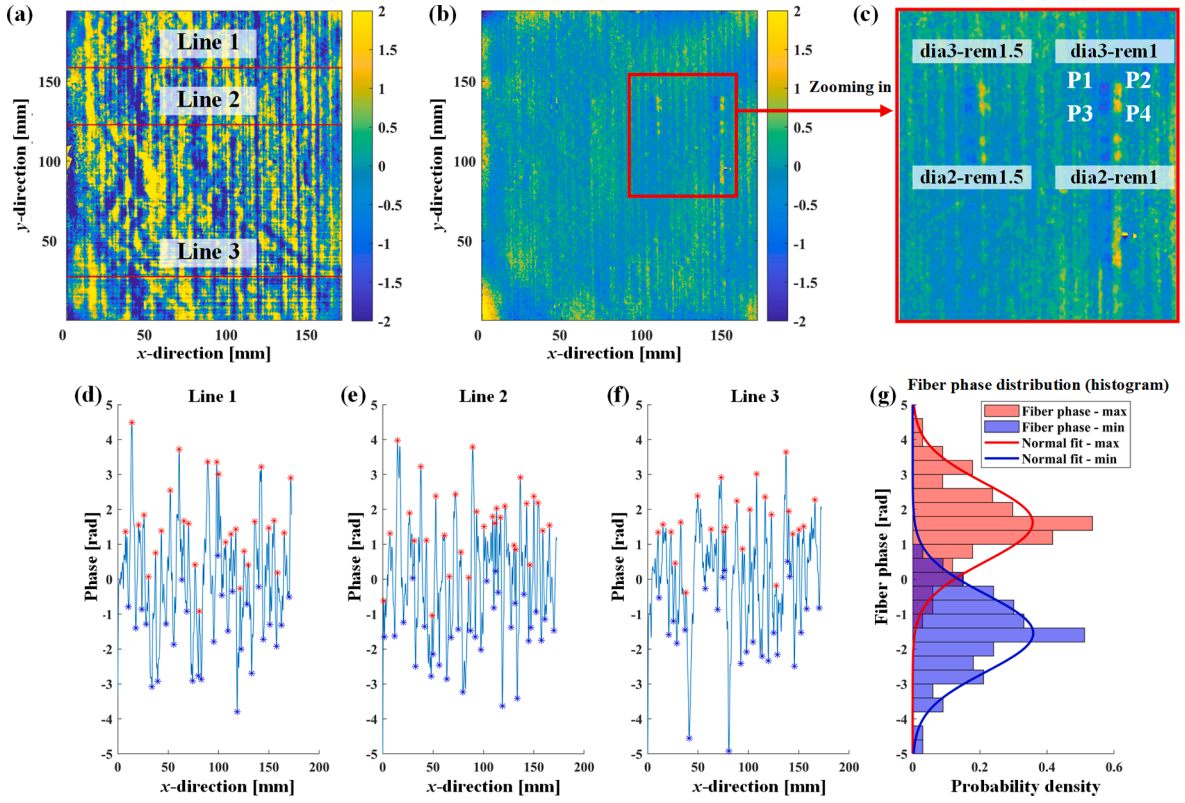

Fig. 4. (a) The compensated phase map of the total heating to identify positions of fiber bundles. (b) Compensated phase map (from the shearography pair method) showing the positions of defects. (c) Zooming in on the defect areas. The defects (FBHs) show up as 'blue and yellow' dots in the figure. (d)-(f) Phase changes across Lines 1–3 (horizontal lines in (a)), local max and min phases marked in red and blue, respectively. (g) A histogram of local max and min phases to show fiber-related phase distribution (with a fitted normal distribution overlaid for visual confirmation). Phase units in rad. (For interpretation of the references to colour in this figure legend, the reader is referred to the web version of this article.)

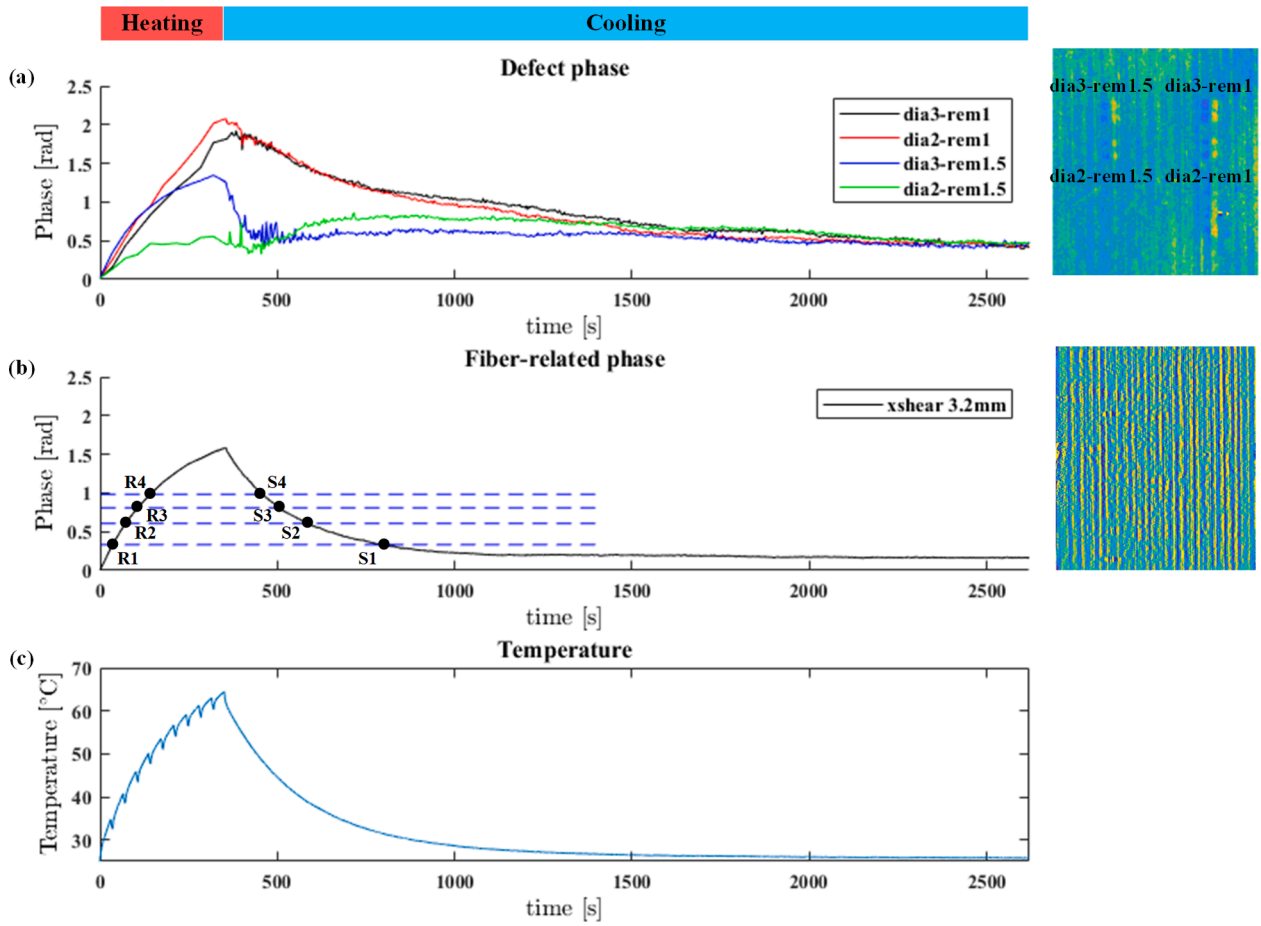

Fig. 5. (a) The evolution of the defect-induced phase with time of the four twin defects. (b) The evolution of fiber-induced phase with time. (c) Overall transient temperature with time measured by IR camera. 10 isolated temperature jumps in the heating correspond to 10 heating cycles. Phase units in rad, 1 rad corresponds to 13.2 με.

compensated phase map from shearography pair and the corresponding defect area are shown in Fig. 4 (b-c). To identify the defect-induced phase, we first looked at four twin defects, which are dia3-rem1, dia2-rem1, dia3-rem1.5 and dia2-rem1.5, respectively. Each FBH in the shearography phase map is seen as a 'butterfly' with a phase min and max, resulting in two 'blue and yellow' dots in Fig. 4. So for each twin defect (for example dia3-rem1, two FBHs of the same size and at the same depth), it results in four small dotted-shape areas (P1-P4). The defect signal is calculated as (-P1-P3 + P2 + P4)/4 because the phase values are negative in P1 and P3 regions, and are positive in P2 and P4 regions. This average operation was performed on each compensated phase map in the time sequence so that the evolution of defect-induced deformation during the inspection can be achieved, as shown in Fig. 5 (a).

3.2. The analysis of fiber-related and defect-induced phases

The evolution of the defect-induced phase with time for the four defects (dia3-rem1, dia2-rem1, dia3–rem1.5 and dia2-rem1.5) is shown in Fig. 5(a). The heating was in 10 cycles of 30 s from 0 to 350 s and then cooling till 2600 s. First, during heating, the defect signal (dia3-rem1 and dia2-rem1) increases up to the max of approximately 2 rad. The maximum signal is close to the moment at the end of the heating. Further in time, the defect signal decreases. The evolution of the fiber-related phase with time is shown in Fig. 5(b). The localized fiber noise behaves similarly to the defect signal in time (first it increases, then decreases). The maximum fiber phase change is around 1.5 rad, which is comparable to the defect signal during the inspection. Therefore when both the defect signal and fiber noise are maximal (Fig. 4(a)), no defects are detected. The transient temperature of the front surface is shown in Fig. 5(c). The temperature increase is about 40 °C. The 10 isolated temperature jumps in the heating correspond to 10 heating cycles of 30 s with 5 s gaps. These gaps in the heating allow the shearography measurement to be taken in between (without overexposing the camera to the light of the lamps).

3.3. Shearography pairs for reliable defect detection

The proposed approach – shearography pair – is a way to find the pairs of the reference and signal interferograms from the heating/cooling sequence to result in the minimum fiber noise. It includes 3 main steps (Fig. 6):

- Step 1 (Fig. 6 (1.1–1.3)): The speckle interferograms are continuously recorded before heating, after each cycle of heating, and during cooling. The recorded shearographic data are processed sequentially through temporal phase shifting (four-step), phase filtering and unwrapping to obtain phase stacking (sequential build-up). Phase compensation is needed to remove the phase change due to global deformation (Fig. 3(c-d)).
- Step 2 (Fig. 6 (2.1–2.5)): Fiber deformation phase is extracted from the obtained phase stack. First, fiber bundle positions are extracted by identifying the positions of local maxima and minima along the three red lines from the total heating phase map. Then fiber phase is calculated according to Eq. (1). The evolution of fiber-induced phase in time is obtained (Fig. 6 (2.5)).

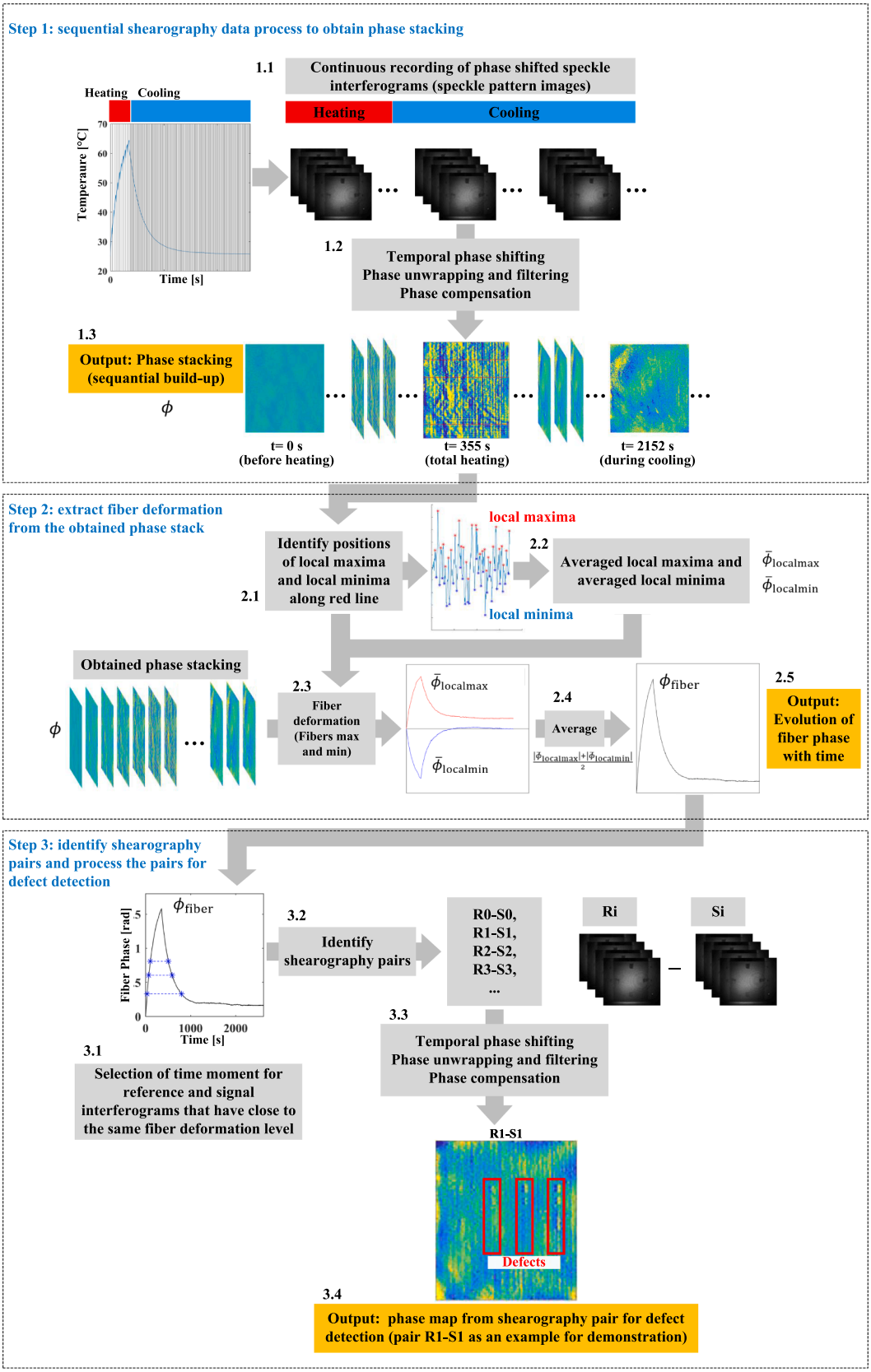

Fig. 6. Flowchart for the selection of shearography pairs.

- Step 3 (Fig. 6 (3.1–3.4)): Once the evolution of fiber phase in time is achieved, shearography pairs can be identified through the selection of time moment for the reference and signal interferograms that have close to the same fiber deformation level. In other words, for each reference state (reference sets of speckle interferograms) before and during the heating, the corresponding signal state (signal sets of speckle interferograms) are searched in the cooling that has close to the same fiber deformation (e.g., R1 and S1 in Fig. 5(b)). The operation for searching the shearography pairs is summarised as:

$$(R_i, S_i)|S_i = \mathrm{argmin}_{S_j^* \in \{S_j^*\}} \left| \phi_{R_i}^{\mathrm{fiber}} - \phi_{S_j^*}^{\mathrm{fiber}} \right|, \; R_i \in \{\boldsymbol{R_i}\}, \; i = 0, 1, 2, 3, 4\cdots \tag{2}$$

Where $\{\boldsymbol{R_i}\}$ is the set of the reference speckle interferograms before heating (R0) and in the heating (R1, R2…) and $\left\{\boldsymbol{S_j^*}\right\}$ is the set of the signal speckle interferograms in the cooling, (R_i, S_j) represents the shearography pair that yields minimum fiber noise. An appropriate code using the min function in MATLAB has been developed for the operation of searching the shearography pairs (1-second runtime for 600 + values).

The selected pairs of the reference and signal speckle interferograms are processed through temporal phase shifting (four-step), phase filtering and unwrapping, and phase compensation. The obtained phase maps yield minimum fiber noise for defect detection (e.g., Fig. 6 (3.4)).

The results show that those shearography pairs exist at the moments when the temperature of the front surface of the specimen during heating is close to the same value during cooling (Fig. 5(b-c)).

It is acknowledged that here the defect signal is not taken into account when searching for the shearography pairs. The reason and the effect will be discussed in Section 4.2.

4. Results and discussion

In this section, the inspection results from the shearography pair method are presented and compared with the ones from conventional shearography practice (Section 4.1) and with FFT- and PCA-based signal processing algorithms (Section 4.2). The FFT and PCA are not the core of the paper, they are used to compare the performance of the developed shearography pair method. Additionally, a comparison of shearography pair and conventional sequential phase build-up is given (Section 4.3).

4.1. Shearography pair method compared with conventional shearography practice

First, an overall comparison of conventional shearography practice and shearography pair results is made. Fig. 7(b) and 7(c) represent the worst cases with the deformation during heating or cooling which satisfy the conventional shearography practice of "one before and another after the object is slightly deformed" [49,50]. However, these results are not useful as the fiber-induced deformation is higher than or comparable to the expected signal from defects. On the other hand, successful detection of defects in the same specimen during the same test is possible (Fig. 7 (d)) using the shearography pair of R0 (the reference state before heating, normal reference used in shearography) and S0 (the corresponding signal state in the cooling, selected using the shearography pair method). The fiber phases of R0 and S0 selected are different due to accumulative noise in the sequential phase build-up. Signal-to-noise ratio (SNR), shown in Fig. 7(b-d), is calculated as a ratio of defect signal from dia3-rem1 to one standard deviation (STD) of the background phase signals in a healthy region. The one STD of the background phases is used to indicate the noise level. It can serve as a baseline to compare with defect signals. The defect signals from the FBHs (diameters of 0.6–3 mm with remaining thickness of 1 mm) and noise level are given in Fig. 7(f). The unit of phase is radian. The noise level from

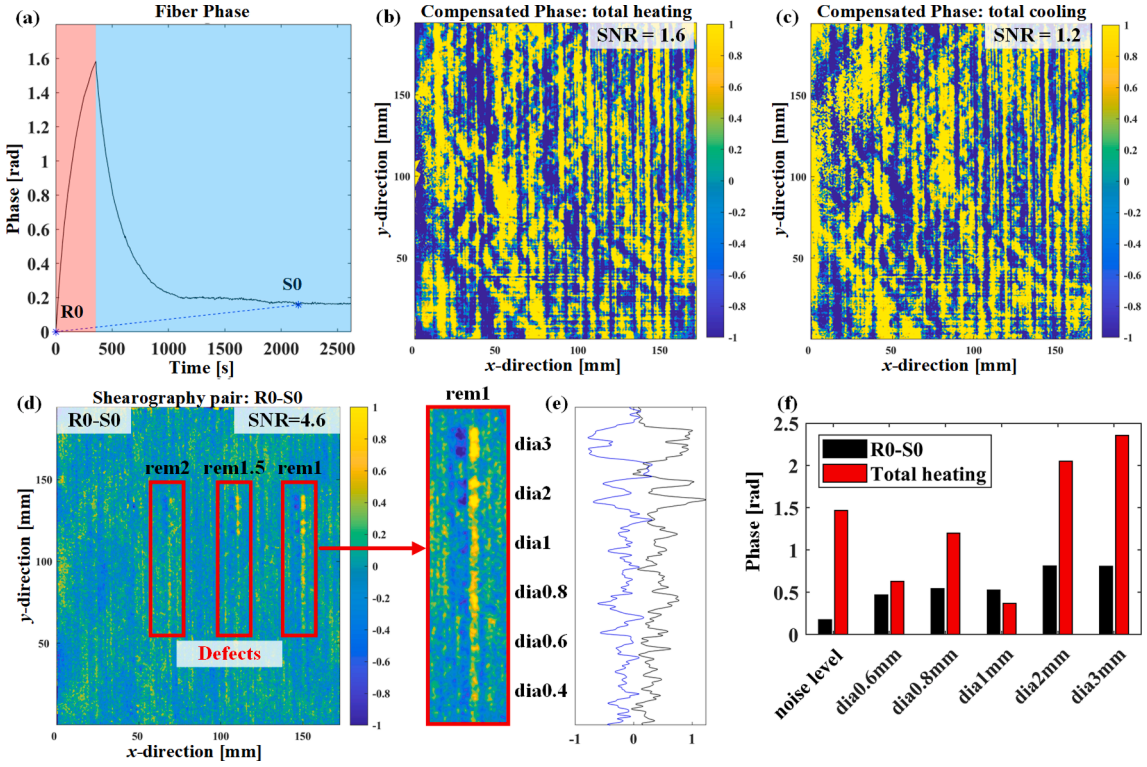

Fig. 7. Comparison of phase maps: (a) fiber phase in time during heating (in red) and cooling (in blue); shearography pair R0-S0 marked. Conventional shearography practice of (b) total heating case and (c) total cooling case; (d) shearography pair R0-S0; (e) cross-sections along *y*-direction with the signals from the FBHs (rem 1); (f) noise level and defect signals from the FBHs (dia: 0.6–3 mm, rem: 1 mm). Phase units in rad, 1 rad corresponds to 13.2 με. (For interpretation of the references to colour in this figure legend, the reader is referred to the web version of this article.)

shearography pair R0-S0 (0.17 rad) is smaller than that from conventional shearography practice of total heating (1.47 rad). Besides, for the shearography pair case, the SNR from the FBHs (diameter of 0.6–0.8 mm, remaining thickness of 1 mm) ranges from 2.7 to 4.6, which is much higher than the SNR for the total heating case (0.25–1.60). This shows the effect of the shearography pair in reducing the fiber noise.

It takes more than 2000 s to capture the shearography pairs of the reference before heating (R0) and the corresponding signal speckle interferogram (S0), which is time-consuming for the inspection. The inspection results of other found pairs are shown in Fig. 8, where the references from R1 to R4 are at 1st to 4th cycles of heating and the corresponding signal states from S1 to S4 are in the cooling (Fig. 5(b)). The time axis in Fig. 8 (a, e, i, m) is the same as Fig. 7(a), which is 10 cycles of 30 s heating from 0 to 350 s and then cooling till 2600 s. The inspection results of shearography pairs (R1-S1 to R4-S4) are shown in Fig. 8 (b, f, j, n), and the results from conventional practice (R0-S1 to R0-S4) are in Fig. 8 (c, g, k, o). SNR is calculated as a ratio of defect signal from dia3-rem1 to one STD of the background phase signals in the healthy region. The shearography pairs provide results of good quality (SNR of 2.1–3.5) for defect detection, which are faster in inspection compared to the shearography pair of S0–R0 (500–800 s for capturing pairs R1-S1 to R4-S4 and 2000 s for capturing pair R0-S0).

The noise levels and defect signals of the FBHs (diameter of 0.6–3 mm, remaining thickness of 1 mm) from shearography pairs (R1-S1 to R4-S4) and conventional practice (R0-S1 to R0-S4) respectively are shown in Fig. 8(d, h, l, p). The noise level from shearography pairs (0.31–0.38 rad) is smaller than that from conventional practice (0.35–1.15 rad). For shearography pairs (R1-S1 to R4-S4), the defect signals of the FBHs (diameter of 0.6–0.8 mm, remaining thickness of 1 mm) are higher than noise level; while for conventional practice (R0-S2 to R0-S4), the signals from those defects are lower than the corresponding noise level. Besides, the defects of diameters of 2–3 mm (rem-1.5 mm) are detectable from shearography pairs (Fig. 8 (b, f, j, n)) while they are barely detected from conventional practice (Fig. 8 (c, g, k, o)). In general, shearography pairs offer better results than conventional practice.

Since the defect signal is not considered when searching for the shearography pairs, in practical experiments the efficacy of defect detection may vary using different shearography pairs (Fig. 8(d, h, l, p)). This is because the phase of the defects may be affected when eliminating the fiber noise (Fig. 8(d, h, l, p)). For this study, we applied heating of 300 s in total, which gives a temperature rise of about 40 °C for defect detection and the thermal penetration depth (Fig. 9) is much larger than the specimen thickness (4 mm). So it is assumed that defect deformation is sufficient for shearography NDI using different shearography pairs. Hence we only minimise the fiber noise and do not

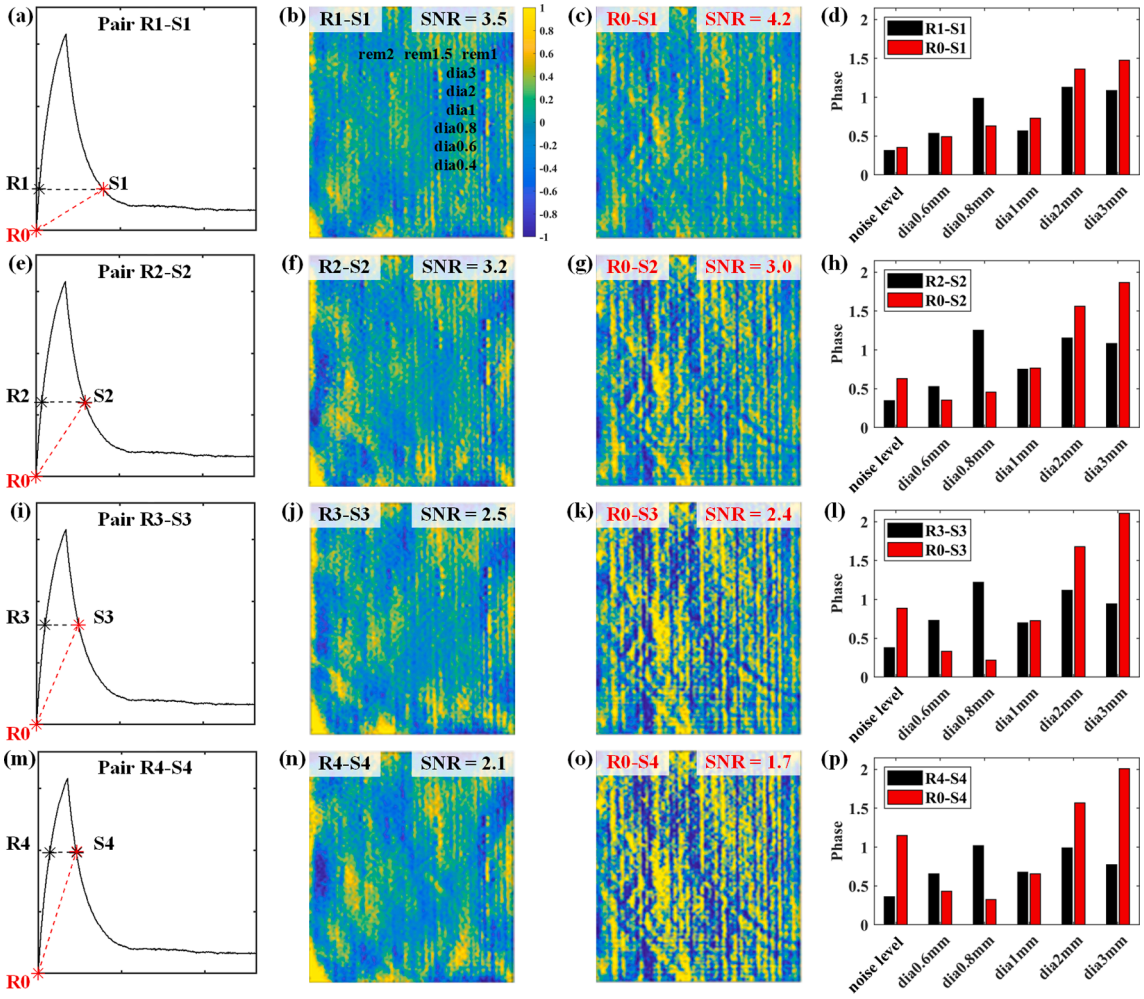

Fig. 8. Comparison of inspection results from various shearography pairs and conventional shearography practice. (a, e, i, m): R0 is the reference before the heating, R1 to R4 are references after the 1st to 4th cycles of heating, S1 to S4 are the corresponding signal states to R1-R4, respectively. The time axis is the same as in Fig. 7 (a). (b, f, j, n) are phase maps with shearography pairs from R1-S1 to R4-S4; (c, g, k, o) are phase maps with conventional shearography practice from R0-S1 to R0-S4. (d, h, l, p) are the noise levels and defect signals from the FBHs (dia: 0.6–3 mm, rem: 1 mm) for shearography pairs (R1-S1 to R4-S4) and conventional practice (R0-S1 to R0-S4). Phase units in rad, 1 rad corresponds to 13.2 με.

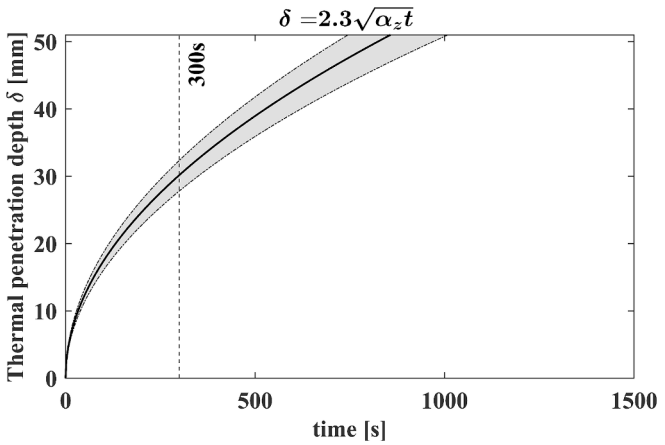

Fig. 9. Thermal penetration depth of the used CFRP laminate, the grey region indicates a 15 % variation in thermal diffusivity in the through-thickness direction ($\alpha_z \approx 0.57 \times 10^{-6}$ m^2/s).

maximise the defect-induced signal. As it is shown in the results in Figs. 7-8, this assumption is valid.

4.2. Comparison with FFT and PCA techniques

We also compared the shearography pair method with FFT- and PCA-based signal processing algorithms for the same datasets. The FFT and PCA algorithms were applied for shearography data (phase maps) in time according to [36,37,39,40]. The FFT results (Fig. 10(a, d)) are presented for the lowest frequency component and the PCA results (Fig. 10(b, e)) are presented for the first principal component as they are most informative for defect detection while other frequency components (FFT) and other principal components (PCA) contain little information about the defects. The shearography pair results also show good performance in those comparisons (Fig. 10). The defects of diameters of 2–3 mm (rem-1.5 and 2 mm) that are barely detected in Fig. 10(a-b) are detected from shearography pair R1-S1 (Fig. 10(c)). Those defects are detectable in Fig. 10(d-f). Readers can make their own decision on which technique (shearography pair method, FFT or PCA) is better regarding the detection efficacy in small mm and sub-mm defects. Nevertheless, it is good to note that for FFT and PCA, hundreds of datasets need to be processed every time; while for shearography pair method, when the evolution of fiber-induced phase is obtained for once, only one pair of datasets is needed, i.e. reference and signal speckle interferograms respectively.

4.3. Shearography pair vs sequential build-up

A comparison of shearography pair and conventional sequential build-up of the phase (or so-called phase stacking) is given in Fig. 11. The compensated phase maps by sequential build-up (500 + phase increments from R0 to S0) and by the pair R0-S0 are shown in Fig. 11(b) and 11(c), respectively. Here we show that the detection efficacy using the compensated phase map of the shearography pair is better than using the one of sequential build-up. The difference in detection is due to accumulative noise in the sequential phase-calculation process. It was experimentally found that the accumulative noise in the sequential phase build-up is around ± 0.4 rad (up to 500 + phase increments, one

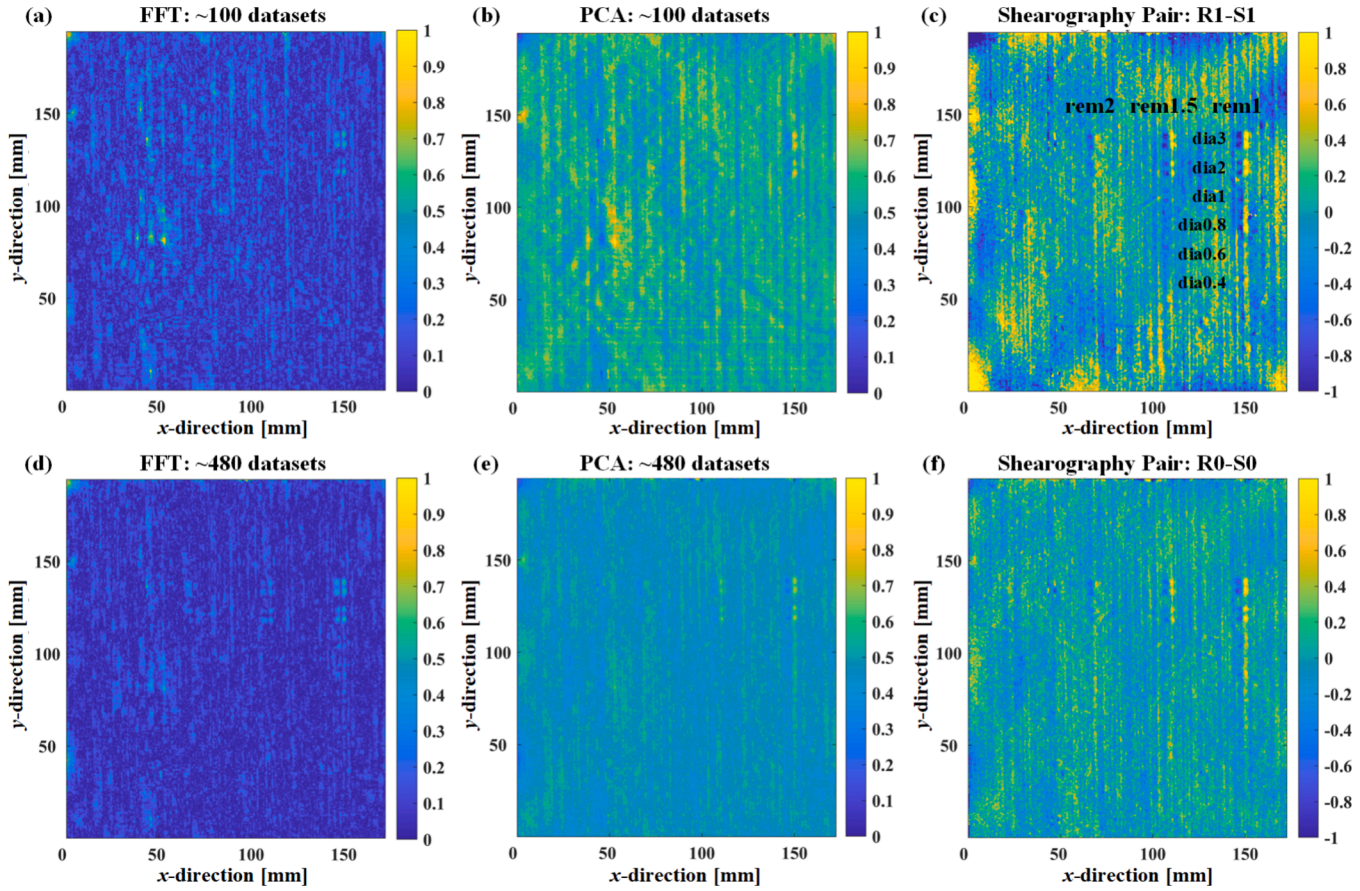

Fig. 10. Shearography pair method compared with FFT and PCA. (a) and (b) are FFT (amplitude of the lowest frequency component) and PCA (first principal component) results by processing around 100 datasets in between R1 and S1, (c) is the shearography pair result of R1-S1; (d) and (e) are FFT and PCA results by processing around 480 datasets in between R0 and S0, (f) is the shearography pair result of R0-S0.

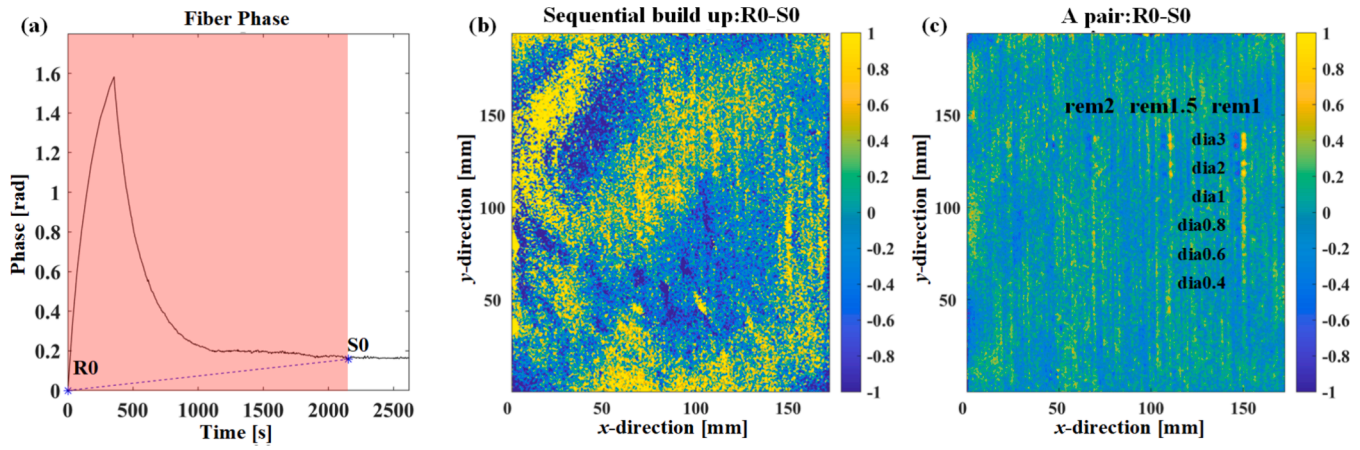

Fig. 11. Comparison of shearography phase calculated by using one pair and sequential build-up. The compensated phase maps by (b) sequential build-up (500 + phase increments) and (c) pair R0-S0.

STD) and the noise using the pair is around ± 0.08 rad (one STD). However, it should be noted that the sequential phase build-up is applicable to measure a larger deformation range (e.g., hundreds to thousands of rad in phase) compared to using one pair. Additionally, we tested the shearography pair method with different shearing distances (2.0–5.7 mm), and it showed repeatable detection as in Fig. 11(c).

5. Conclusions

In this work, the new shearography pair method has been proposed and developed to reduce the fiber noise for the detection of small mm and sub-mm defects in fiber-reinforced composites. Shearography pairs are the pairs of reference and signal sets of phase-shifted speckle interferograms that yield minimum fiber noise. The defect detection efficacy of the proposed method has been studied and compared with conventional shearography practice and with FFT- and PCA-based signal processing algorithms. Overall, the shearography pair method has the advantages of less fiber noise, improved inspection results, and being faster with a reduced number of datasets. With the proposed method and the current setup, at a defect depth of 1 mm, defects of 0.6 to 3.0 mm in size are detected, while at the depths of 1.5 and 2.0 mm, defects of 2 and 3 mm in size are detected. Sub-mm defects of 0.6–0.8 mm in size are detected (at defect depth of 1 mm; Fig. 7(d-f), 8 and 11(c), a supplementary video on experimental results is also available), which are the smallest defects detected with thermal-based shearography (when macroscopic inspection is considered, excluding microscopy applications). The evolution of fiber induced phase is needed for the selection of shearography pairs. The results show that those pairs exist at the moments when the temperature of the front surface of the specimen during heating is close to the same value during cooling (this can be helpful for practical shearography inspection).

The conclusions are achieved with the test CFRP specimen using flat bottom holes as reference defects and in the lab environment. In general, real inspection is challenging due to the problems of vibrations, airflows, and non-uniform heating. The detectability of this method in the presence of actual defects such as real delaminations and cracks in composites will be investigated in the future, e.g., by developing FEM-assisted approaches to model delaminations and cracks, and to guide shearography inspection (including optimization of loading parameters to improve the detection). Future work could take defect signals into account when determining shearography pairs for defect detection. The shearography pair method would also be used to inspect smart structures with embedded sensors (e.g., CNT-doped strips and grids in composite laminates) that may raise similar issues as fiber noise.

CRediT authorship contribution statement

Nan Tao: Writing – review & editing, Writing – original draft, Visualization, Validation, Software, Methodology, Investigation, Formal analysis. **Roger M. Groves:** Writing – review & editing, Supervision, Project administration, Funding acquisition. **Andrei G. Anisimov:** Writing – review & editing, Visualization, Supervision, Software, Conceptualization.

Declaration of competing interest

The authors declare that they have no known competing financial interests or personal relationships that could have appeared to influence the work reported in this paper.

Acknowledgment

This research was performed as part of the Horizon Europe COMPECO project (grant agreement 101079250). The authors would like to thank the Air Force Institute of Technology from Warsaw, Poland and Optrion, Belgium for providing access to commercial shearography instrumentation for benchmark tests, and Dr. Morteza Moradi from TU Delft for his kind help in the FFT and PCA algorithms. The authors would also like to thank Dr. Luis Garza-Soto from TU Delft for his feedback on the manuscript.

Appendix A. Supplementary data

Supplementary data to this article can be found online at https://doi.org/10.1016/j.measurement.2025.117980.

Data availability

Data will be made available on request.

References

[1] M.E. Ibrahim, Nondestructive evaluation of thick-section composites and sandwich structures: A review, Compos. Part A Appl. Sci. Manuf. 64 (2014) 36–48.
[2] W. Nsengiyumva, S. Zhong, J. Lin, Q. Zhang, J. Zhong, Y. Huang, Advances, limitations and prospects of nondestructive testing and evaluation of thick composites and sandwich structures: A state-of-the-art review, Compos. Struct. 256 (2021) 112951.
[3] E. Greene, Inspection techniques for marine composite construction and NDE, Rep. No. SSC-463, United States Sh. Struct. Committee, Washington, DC (2012).
[4] CMH-17-3G, Composite Materials Handbook, Volume 3 - Polymer Matrix Composites - Materials Usage, Design, and Analysis (CMH-17), SAE International, 2012.

[5] M. Inês Silva, E. Malitckii, T.G. Santos, P. Vilaça, Review of conventional and advanced non-destructive testing techniques for detection and characterization of small-scale defects, Prog. Mater. Sci. 138 (2023) 101155.
[6] R.M. Groves, Inspection and Monitoring of Composite Aircraft Structures, in: P.W. R. Beaumont, C.H. Zweben (Eds.), Compr, Compos. Mater. II, Elsevier, Oxford, 2018, pp. 300–311.
[7] D. Francis, R.P. Tatam, R.M. Groves, Shearography technology and applications: a review, Meas. Sci. Technol. 21 (2010) 102001.
[8] N. Tao, A.G. Anisimov, R.M. Groves, Shearography non-destructive testing of thick GFRP laminates: Numerical and experimental study on defect detection with thermal loading, Compos. Struct. 282 (2022) 115008.
[9] J.W. Newman, Shearography Nondestructive Testing of Composites, in: P.W. R. Beaumont, C.H. Zweben (Eds.), Compr, Compos. Mater. II, Elsevier, Oxford, 2018, pp. 270–290.
[10] N. Tao, A.G. Anisimov, R.M. Groves, FEM-assisted shearography with spatially modulated heating for non-destructive testing of thick composites with deep defects, Compos. Struct. 297 (2022) 115980.
[11] L. Ma, C. Liu, J. Han, A. Wen, B. Liu, J. Zheng, Delamination defects in composite hydrogen storage cylinders: CT scanning and shearography measurement, Int. J. Hydrogen Energy 97 (2025) 140–149.
[12] N. Tao, E. van Duijn, L. Vos, I. Steeman, R.M. Groves, K. Keune, P. Noble, A. G. Anisimov, Assessing the structural integrity of the wax-resin lining of The Night Watch using 3D shearography, J. Cult. Herit. 72 (2025) 169–179.
[13] L. Zhang, Z.W. Tham, Y.F. Chen, C.Y. Tan, F. Cui, B. Mutiargo, L. Ke, Defect imaging in carbon fiber composites by acoustic shearography, Compos. Sci. Technol. 223 (2022) 109417.
[14] Z.W. Tham, S. Sampath, Y.F. Chen, B. Mutiargo, L. Zhang, Non-contact defect imaging of carbon fiber composites using laser excited acoustic shearography, Compos. Sci. Technol. 257 (2024) 110796.
[15] S. Sampath, Z.W. Tham, Z. Zhang, Y.F. Chen, A.K.H. Cheong, L.T. Chew, D.H. L. Seng, L. Zhang, Non-contact imaging of microcracks in metallic coatings using laser excited acoustic shearography, Measurement 245 (2025) 116609.
[16] L. Zhang, Y.F. Chen, H. Liu, B. Russell, Z.W. Tham, L. Ke, U.M. Velayutham, In-situ real-time imaging of subsurface damage evolution in carbon fiber composites with shearography, Compos. Commun. 32 (2022) 101170.
[17] Y.Y. Hung, L.X. Yang, Y.H. Huang, Non-destructive evaluation (NDE) of composites: digital shearography, in: V.M. Karbhari (Ed.), Non-Destructive Eval, Woodhead Publishing, Polym. Matrix Compos., 2013, pp. 84–115.
[18] B. Guo, X. Zheng, M. Gerini-Romagnoli, L. Yang, Digital shearography for NDT: Determination and demonstration of the size and the depth of the smallest detectable defect, NDT E Int. 139 (2023) 102927.
[19] X. Xie, Z. Zhou, Shearographic nondestructive testing for high-pressure composite tubes, SAE Technical Paper 2018-01-1219, 2018.
[20] X. Xie, Z. Zhou, H. Kolambe, A. Bothe, Non-Destructive Evaluation for High-Pressure Composite Tubes using a Hybrid Approach, SAE Technical Paper 2019-01-1268, 2019.
[21] H.M. Shang, F.S. Chau, C.J. Tay, S.L. Toh, Estimating the depth and width of arbitrarily-oriented disbonds in laminates using shearography, J. Nondestruct. Eval. 9 (1990) 19–26.
[22] J. Gryzagoridis, D. Findeis, N.B. Vukeya, Vacuum excitation in shearographic NDT, Insight-Non-Destructive Test. Cond. Monit. 49 (2007) 98–101.
[23] F. Yang, X. Ye, Z. Qiu, B. Zhang, P. Zhong, Z. Liang, Z. Sun, S. Zhu, The effect of loading methods and parameters on defect detection in digital shearography, Results Phys. 7 (2017) 3744–3755.
[24] N. Tao, A. Anisimov, M. Elenbaas, R.M. Groves, Shearography non-destructive testing of a composite ship hull section subjected to multiple impacts, in: Proc. 20th Eur. Conf. Compos. Mater. Compos. Meet Sustain., 2022.
[25] G. De Angelis, M. Meo, D.P. Almond, S.G. Pickering, S.L. Angioni, A new technique to detect defect size and depth in composite structures using digital shearography and unconstrained optimization, NDT E Int. 45 (2012) 91–96.
[26] E. Vikhagen, K. Nelvik, NDT of offshore composite wrap repairs - New technology available, in: E-Journal Nondestruct. Test. Vol. 23(8)., 12th European Conference on Non-Destructive Testing (ECNDT 2018), 2018: pp. 1–6. https://www.ndt.net/?id=22665.
[27] Z. Liu, J. Gao, H. Xie, P. Wallace, NDT capability of digital shearography for different materials, Opt. Lasers Eng. 49 (2011) 1462–1469.
[28] W. Steinchen, L. Yang, G. Kupfer, P. Mäckel, Non-destructive testing of aerospace composite materials using digital shearography, Proc. Inst. Mech. Eng. Part G J. Aerosp. Eng. 212 (1998) 21–30.
[29] N. Tao, A.G. Anisimov, R.M. Groves, Towards safe shearography inspection of thick composites with controlled surface temperature heating, NDT E Int. 139 (2023) 102907.
[30] E.C. Krutul, R.M. Groves, Opto-mechanical modelling and experimental approach to the measurement of aerospace materials using shearography and thermal loading, in: B. Bodermann (Ed.), Model, SPIE, Asp. Opt. Metrol. III, 2011, pp. 434–442.
[31] P.G. Bison, C. Bressan, G. Cavaccini, A. Ciliberto, E.G. Grinzato, NDE of composite materials by thermal method and shearography, in: R.N. Wurzbach, D.D. Burleigh (Eds.), Thermosense XIX An Int. Conf. Therm. Sens. Imaging Diagnostic Appl., SPIE, 1997: pp. 220–229.
[32] C. Garnier, M.L. Pastor, F. Eyma, B. Lorrain, The detection of aeronautical defects in situ on composite structures using non destructive testing, Compos. Struct. 93 (2011) 1328–1336.
[33] R.R. Hughes, B.W. Drinkwater, R.A. Smith, Characterisation of carbon fibre-reinforced polymer composites through radon-transform analysis of complex eddy-current data, Compos. Part B Eng. 148 (2018) 252–259.
[34] Q. Yi, P. Wilcox, R. Hughes, Modelling and evaluation of carbon fibre composite structures using high-frequency eddy current imaging, Compos. Part B Eng. 248 (2023) 110343.
[35] G. Poelman, S. Hedayatrasa, W. Van Paepegem, M. Kersemans, Enhanced thermographic inspection of woven fabric composites by k-space filtering, Compos. Part B Eng. 252 (2023) 110508.
[36] M. Moradi, M.S. Safizadeh, Edge disbond detection of carbon/epoxy repair patch on aluminum using thermography, Compos. Sci. Technol. 179 (2019) 41–53.
[37] M. Moradi, M.S. Safizadeh, Detection of edge debonding in composite patch using novel post processing method of thermography, NDT E Int. 107 (2019) 102153.
[38] P. Pfeffer, L. Wachter, D. Hoffmann, C. Kolb, G. Schober, M. Bastian, A study of multifrequent shearographic lock-In measurements of CFRP, in: Int. Symp. Struct. Heal. Monit. Nondestruct. Test., 2018.
[39] J.-F. Vandenrijt, N. Lièvre, M.P. Georges, Improvement of defect detection in shearography by using principal component analysis, in: K. Creath, J. Burke, J. Schmit (Eds.), Interferom, SPIE, XVII Tech. Anal., 2014.
[40] M. Kirkove, Y. Zhao, P. Blain, J.-F. Vandenrijt, M. Georges, Thermography-inspired processing strategy applied on shearography towards nondestructive inspection of composites, in: P. Lehmann, W. Osten, A.A.G. Jr (Eds.), Opt, SPIE, Meas. Syst. Ind. Insp. XI, 2019.
[41] N. Tao, A.G. Anisimov, R.M. Groves, Shearography with thermal loading for defect detection of small defects in CFRP composites, in: C. Binetury, F. Jacquemin (Eds.), Proc. 21st Eur. Conf. Compos. Mater., The European Society for Composite Materials (ESCM) and the Ecole Centrale de Nantes, 2024, pp. 85–90.
[42] D. Akbari, N. Soltani, M. Farahani, Numerical and experimental investigation of defect detection in polymer materials by means of digital shearography with thermal loading, Proc. Inst. Mech. Eng. Part B J. Eng. Manuf. 227 (2013) 430–442.
[43] ASTM E2581, Standard practice for shearography of polymer matrix composites, sandwich core materials and filament-wound pressure vessels in aerospace applications, 2014.
[44] P.A. Howell, Nondestructive evaluation (NDE), Methods and Capabilities Handbook (2020).
[45] A.G. Anisimov, M.G. Serikova, R.M. Groves, 3D shape shearography technique for surface strain measurement of free-form objects, Appl. Opt. 58 (2019) 498–508.
[46] A.G. Anisimov, B. Müller, J. Sinke, R.M. Groves, Analysis of thermal strains and stresses in heated fibre metal laminates, Strain 54 (2018) e12260.
[47] Klein Tools, Emissivity Chart. Accessed April 29, 2025., (n.d.). https://data.kleintools.com/sites/all/product_assets/documents/brochures/klein/EmissivityChart.pdf.
[48] D.C. Ghiglia, M.D. Pritt, Two-dimensional phase unwrapping: theory, algorithms, and software, Wiley, New York, 1998.
[49] Y.Y. Hung, H.P. Ho, Shearography: An optical measurement technique and applications, Mater. Sci. Eng. R Reports 49 (2005) 61–87.
[50] Y.Y. Hung, Shearography: a new optical method for strain measurement and nondestructive testing, Opt. Eng. 21 (1982).